



Structure, vibrations and electronic transport in silicon suboxides: Application to physical unclonable functions

C. Ugwumadu^{a,*}, K.N. Subedi^{a,*}, R. Thapa^a, P. Apsangi^b, S. Swain^c, M.N. Kozicki^b, D. A. Drabold^{a,*}

^a Department of Physics and Astronomy, Nanoscale and Quantum Phenomena Institute (NQPI), Ohio University, Athens 45701, OH, USA

^b School of Electrical, Computer, and Energy Engineering, Arizona State University, Tempe 85287, AZ, USA

^c School for Engineering of Matter, Transport and Energy, Arizona State University, Tempe 85287, AZ, USA

ARTICLE INFO

Keywords:

PUF
Silicon
Suboxides
Molecular dynamics
DFT
Tersoff

ABSTRACT

This work focuses on the structure and electronic transport in atomistic models of silicon suboxides ($a\text{-SiO}_x$; $x = 1.3, 1.5$ and 1.7) used in the fabrication of a Physical Unclonable Function (PUF) devices. Molecular dynamics and density functional theory simulations were used to obtain the structural, electronic, and vibrational properties that contribute to electronic transport in $a\text{-SiO}_x$. The percentage of Si-[Si₁, O₃] and Si-[Si₃, O₁], observed in $a\text{-SiO}_{1.3}$, decrease with increasing O ratio. Vibrations in $a\text{-SiO}_x$ showed peaks that result from topological defects. The electronic conduction path in $a\text{-SiO}_x$ favored Si-rich regions and Si atoms with dangling bonds formed charge-trapping sites. For doped $a\text{-SiO}_x$, the type of doping results in new conduction paths, hence qualifying $a\text{-SiO}_x$ as a viable candidate for PUF fabrication as reported by Kozicki [Patent-Publication-No.: US2021/0175185A1, 2021].

1. Introduction

Nowadays, with advancements in the Internet of Things (IoT), data confidentiality and authentication have become as important as data storage. Current practices of providing a secure memory or authentication using electrically erasable programmable read-only memory (E²PROM) or static random-access memory (SRAM) are expensive both in terms of design and power consumption [1,2]. Using a physical key, commonly known as Physical Unclonable Function (PUF), is a promising alternative for secret key storage without requiring any expensive hardware [3]. PUFs are physical observables derived from complex physical structures in such a way that each realization of a PUF produces a stable and unique identifier that cannot be cloned, guessed, stolen, or shared. This is because the keys are generated only when required and never stored in any system, thus providing advanced security. As is the case for all solid-state devices, the performance of a PUF depends on the material used in its design. Materials that have been proposed, studied, and used in fabricating PUFs include silicon [4], carbon nanotubes [5], and more recently, silicon suboxides [6].

Silicon suboxides ($a\text{-SiO}_x$) have become an important material in solid-state electronics fabrication, not only because of their availability,

cost-effective production, and industry familiarity but also for their appreciable physical and chemical stability. These properties qualified their use as inter-layer dielectrics in the “back end of line” (BEOL) of complementary metal–oxide–semiconductor (CMOS) integrated circuits (IC), active layers in resistive random-access memory (RRAM) cells, gates, fields, pads, and inter-poly oxides in a variety of devices [7–12]. Two electronic conduction modes have been proposed for $a\text{-SiO}_x$ used in resistive device fabrication: (1) Field-driven diffusion of the metal ions from metal contacts in the material [13,14] and (2) formation of conduction pathways by silicon-rich regions in the material [15,16]. Non-volatile memory devices based on resistive switching, have emerged as promising alternatives to conventional charge storage-based memory technologies, like E²PROM and flash memory. This is due to factors that include device simplicity, low power consumption, high write/erase speeds, and high-density integration [17–19]. These advanced devices operate by switching conductivity between high and low resistance states via applied voltage to a metal-insulator–metal (M-I-M) memory cell. In addition, silicon oxides have been applied in novel non-von Neumann information processing systems, such as neuromorphic systems based on RRAM “synapses” [20].

Returning to the global need for secure data handling, even in low-

* Corresponding authors.

E-mail addresses: cu884120@ohio.edu (C. Ugwumadu), ks173214@ohio.edu (K.N. Subedi), drabold@ohio.edu (D.A. Drabold).

<https://doi.org/10.1016/j.nocx.2023.100179>

Received 14 December 2022; Received in revised form 2 March 2023; Accepted 14 March 2023

Available online 23 March 2023

2590-1591/© 2023 The Authors. Published by Elsevier B.V. This is an open access article under the CC BY-NC-ND license (<http://creativecommons.org/licenses/by-nc-nd/4.0/>).

cost and low-power devices on the IoT, the inherent randomness in the local conformation of a-SiO_x makes it a promising candidate for PUFs. An implementation of a PUF device using SiO_x and a schematic representation of the thin film coatings on a Si substrate are shown in Fig. 1 [LEFT] and [RIGHT] respectively. The design involves plasma-enhanced chemical vapor (PECVD) depositions of a 7 nm-thick layer of silicon suboxide sandwiched between two layers of 100 nm-thick electrochemically-inactive Ni electrodes on the Si substrate. Discussions on the fabrication process and performance of the SiO_x-based PUFs are provided in Sect. S1 of the Supplementary material and in Ref. [6]. Given the ease of its fabrication and the need for improved performance of these SiO_x-based PUFs, an atomistic description of SiO_x and its influence on the electronic transport in these suboxides is essential. This work, which builds upon the preliminary results obtained by one of us (K. N. Subedi [21]), aims at understanding the underlying complexity in the structural topology and the associated microscopic properties of a-SiO_x and its implication on electronic transport within its network. This was achieved from the analysis of an extensive ensemble of structural models generated from molecular dynamics (MD) simulations that involve sampling of SiO_x configuration space, followed by energy minimization of the models using density functional theory (DFT). The rest of this paper is organized as follows: Section 2 provides a detailed description of the computational protocol used to obtain the representative models of silicon suboxides. Section 3 discusses the results of this work and it is divided into subsections. Section 3 (A) provides a detailed analysis of the atomic structure of a-SiO_x for $x = 1.3, 1.5,$ and 1.7 . Section 3 (B) is devoted to the lattice dynamics of the suboxides via the vibrational density of states, inverse participation ratio, bond stretching-bending character, and phase quotient. Section 3 (C) then explores the electronic structure and electron-transport properties of these oxides. A novel method to compute space-projected conductivity (SPC) [22] is briefly discussed and used to visualize the conduction-active pathways in the material. Section 4 presents conclusions.

2. Computational details

The quench-from-melt scheme [23] used in generating the a-SiO_x models requires an extensive exploration of configuration space to avoid getting trapped in unphysical high-energy structures which result from fast quenches. MD simulation was implemented in a slow annealing procedure using a Si-O inter-atomic potential with the Tersoff parameterization of Munetoh and co-workers [24]. This was combined with DFT energy minimization to obtain candidate amorphous models. Tersoff potential is computationally efficient for large system sizes and has been successfully implemented in describing the structural, mechanical, and thermal properties, as well as interface dynamics in silicon and silicon oxides [25–29]. Six initial structures of a-SiO_x were randomly distributed in a cubic supercell with experimental densities [30] as summarized in Table 1.

To simulate melting, 2 independent MD simulations were performed

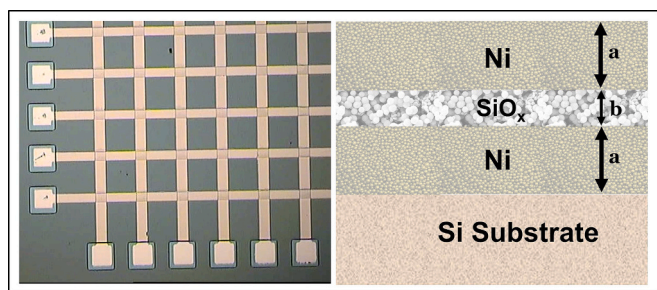


Fig. 1. LEFT: Low-temperature PECVD deposited SiO_x M-I-M device fabricated in 12×12 crossbar arrays. RIGHT: Each intersection contains a $30 \mu\text{m} \times 30 \mu\text{m}$ Ni ($a = 100 \text{ nm}$)– SiO_x ($b = 7 \text{ nm}$) – Ni ($a = 100 \text{ nm}$) device. The M-I-M device fabrication design is displayed in the schematic diagram.

Table 1
Stoichiometries and densities for the a-SiO_x models.

Mol. Formula	N _{Si} / N _O	ρ (g/cc)	L (Å)
SiO _{1.7}	70/ 119	1.99	14.78
	140/ 238		18.62
	74/ 111		15.07
SiO _{1.5}	148/ 222	1.87	18.99
	80/ 104		15.69
SiO _{1.3}	160/ 208	1.68	19.77

for each supercell at 4000 K for a duration of 2 ns. After the first 1 ns, 10 independent liquid configurations were randomly selected after every 0.1 ns interval until the end of the simulation. 20 structures were obtained for each system size described in Table 1 (40 configurations for each stoichiometry considered), hence making a total of 120 configurations. Each sample was then slowly annealed to 300 K at a rate of 0.1 K/ps. Afterwards, the structures were relaxed using DFT energy minimization. The “Large-scale Atomic/Molecular Massively Parallel Simulator” (LAMMPS) software package [31] was used for the MD simulation in the canonical ensemble with a Nosé-Hoover thermostat [32–34] and timestep of 1 fs. DFT calculations were implemented within the “Vienna Ab initio Simulation Package” (VASP) [35], using the generalized gradient approximations (GGA) of Perdew-Burke-Ernzerhof (PBE) [36] in a single \mathbf{k} -point (Γ). A plane-wave basis set with an energy cutoff of 520 eV was fixed for all static calculations and the conjugate-gradient algorithm was applied for the energy minimization.

3. Results and discussions

3.1. Structural topology

The radial distribution function (RDF) for the considered stoichiometries is shown in Fig. 2 (and the insets therein). The equations used in computing the RDF can be found in ref. [37]. The first well-defined peak at $\approx 1.65 \text{ \AA}$ (also observed in glassy SiO₂ [38]) corresponds to Si-O bonds. The hump at $\approx 2.46 \text{ \AA}$ in the SiO_{1.3} and SiO_{1.5} plots corresponds to the increased Si-Si peak (see inset for the Si-Si plot). The average local coordination for a centered Si-atom based on the nearest distance for each atomic pair is displayed in Fig. 3 (a) ($x = 1.3$ (blue), $x = 1.5$ (red), and $x = 1.7$ (green)). The percentage of the dominating tetrahedra Si-[Si₁, O₃] (13) and Si-[Si₃, O₁] (31) in SiO_{1.3} decreased as the oxygen ratio increased to 1.7. In contrast, the fraction of stoichiometric silicon oxide, Si-[Si₀, O₄] (04), has a maximum value in SiO_{1.7}. This confirms that increasing oxygen content in the suboxides recovers the 4-coordinated Si (IV-Si) structure in SiO₂. The high percentage of Si-Si local coordination in SiO_{1.3} (compared to $x = 1.5$ and 1.7) provides it with Si-rich network regions. Fig. 3 (b) shows the trend for all IV-Si. The ratio of Si-[Si₁, O₃] to Si-[Si₃, O₁] was found to be approximately 3:1. This trend is qualitatively comparable to the result obtained by Barranco and co-workers from the X-ray photoelectron spectra (XPS) analysis of the relative amount of tetrahedra silicon found in SiO_x thin films (for $x = 1.3, 1.5,$ and 1.7), which were prepared by evaporation of silicon monoxide [39]. Perevalov and co-workers, through XPS analysis, also showed the presence of these Si oxidation states for non-stoichiometric silicon oxides prepared using the PECVD method [40]. The under-coordinated Si atoms (III-Si and II-Si in Fig. 3(a)) have been reported to exist in both stoichiometric and non-stoichiometric a-SiO₂ as low-energy defects [41,42]. Using the terminology of Ref. [43,44], the major O-vacancy clusters observed were the di-vacancy and tri-vacancy (vacancy chain) geometry. No 3-member Si ring was observed and only the SiO_{1.3} models showed the Y-geometry (see 30 in Fig. 3 (a)). A representative SiO_{1.3} model showing connected Si atoms in the O-vacancy sites is shown in Fig. 4. The large variations in the structural topology of a-SiO_x with the low-energy topological defects provide the structural complexity required in PUF fabrication.

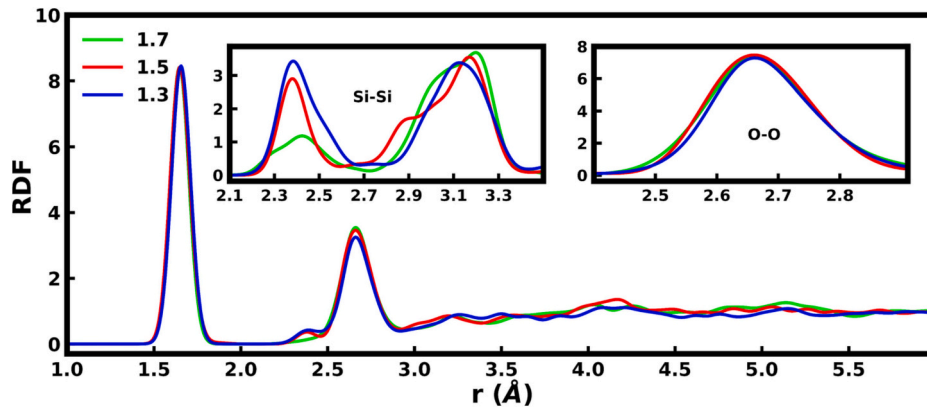


Fig. 2. Radial distribution function (RDF) for the SiO_x models with inset showing the RDF for Si-Si and O-O bonds.

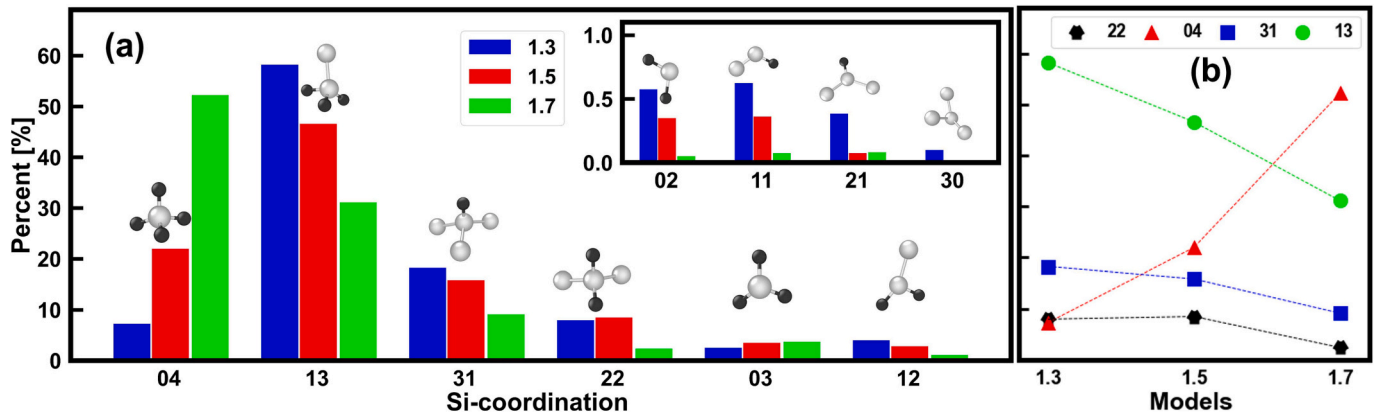


Fig. 3. (a) Local coordination environment for Si atoms (frequencies expressed as percentage). The trend of the fourfold-coordinated Si present in the models is shown in (b). The first index of the x-axis label represents Si and the second index represents the O atom. For example; “04” represents an environment with zero (0) Si and four (4) O bonded to a given Si atom (also written as Si-[Si₀, O₄] in the text). The structures are also represented above the bar charts with the Si and O colored in gray and black respectively.

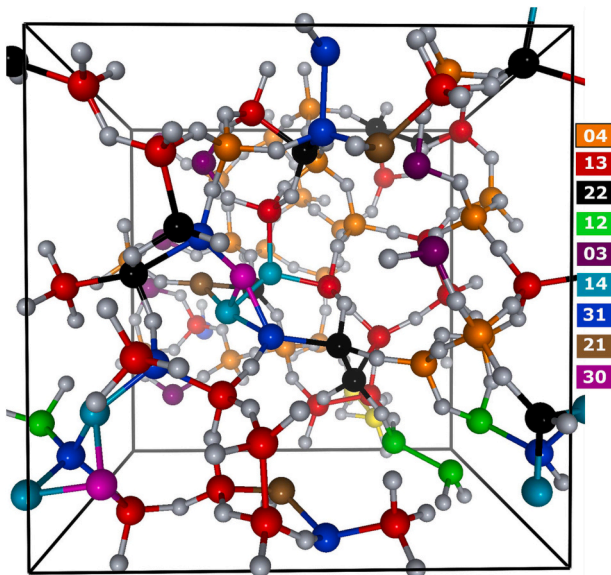


Fig. 4. Representative $\text{a-SiO}_{1.3}$ model showing the Si connections in the network. The color of Si atoms corresponds to their coordination within the first nearest neighbor for each atom. For example; “13” represents an environment with one (1) Si and three (3) O bonded to a given centered Si atom colored in red. All O atoms are colored gray.

3.2. Vibrational properties

Thermal and mechanical properties can be obtained from vibrations in amorphous materials. The Hessian was obtained by calculating the forces resulting from 0.015 Å atomic displacements in six directions ($\pm x$, $\pm y$, $\pm z$), from which the vibrational density of states (VDoS) is obtained as [45]:

$$g(\omega) = \frac{1}{3N} \sum_{i=1}^{3N} \delta(\omega - \omega_i) \quad (1)$$

where N and ω_i present the number of atoms and the eigenfrequencies of the normal modes obtained from the dynamical matrix, respectively. The delta function was approximated by a Gaussian with a standard deviation of 1.5% of the observed maximum frequency. The spatial extent of the normal modes was evaluated via the vibrational inverse participation ratio (VIPR) given as [45]:

$$V(\omega_n) = \frac{\sum_{i=1}^N |u_n^i|^4}{\left(\sum_{i=1}^N |u_n^i|^2\right)^2} \quad (2)$$

u_n^i is displacement vector of i^{th} atom at normal mode frequency ω_n . By definition, a low (high) VIPR represents vibrational modes that are minimally (highly) localized on the atoms. In Fig. 5, the vibrational signature of the a-SiO_x models is compared with those from a 648-atom amorphous silica (a-SiO_2) model from Ref. [46]. Compared to a-SiO_2 ,

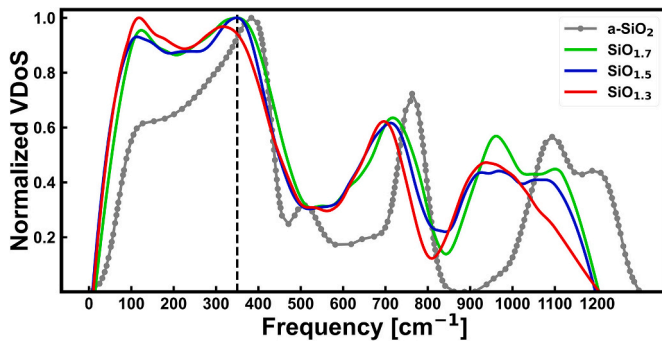


Fig. 5. Total VDoS for the a-SiO_x models are compared with a-SiO₂ spectrum from Ref. [46]. The values of each VDoS were normalized to its maximum value and the black line at 350 cm⁻¹ indicates a peak position in the a-SiO_x models.

the peaks of a-SiO_x appear to have shifted towards the lower frequency regime and no vibration mode was observed beyond 1202 cm⁻¹. This spectral shift is not trivial as the major difference between both spectra is the a-SiO_x peaks at about 350 cm⁻¹ and 900 cm⁻¹. The vibrational gap at 900 cm⁻¹ observed in a-SiO₂ is replaced by fairly intense bands in a-SiO_x. The peak at 900 cm⁻¹ has been observed experimentally in the infrared spectrum of neutron-damaged vitreous silica that produces non-bridging oxygen atoms [47]. Bell and Dean also confirmed that the peak at 900 cm⁻¹ is a consequence of the network defects, that were induced by the presence of these non-bridging oxygen atoms [48]. The VIPR plotted in Fig. 6, Figs.S1 and S2 for a-SiO_{1.3}, a-SiO_{1.5}, and a-SiO_{1.7} respectively, show that a larger fraction of O atoms are localized around 900 cm⁻¹ and at higher frequencies. The Si atoms are mostly localized on a few bands below the vibrational gap around 850 cm⁻¹ and at the low-frequency regime around 31 cm⁻¹. The low-frequency localized Si atoms have unique torsional motions [46]. Also, low energies do not contribute to bond-stretching modes as shown in Fig. 7 (a-c), which represent the stretching and bending character of vibrations defined by [49]:

$$S = \frac{\sum_m |(\mathbf{u}_n^i - \mathbf{u}_n^j) \cdot \hat{\mathbf{r}}_{ij}|}{\sum_m |\mathbf{u}_n^i - \mathbf{u}_n^j|} \quad (3)$$

where, \mathbf{u}_n^i and \mathbf{u}_n^j are the eigenvectors of the nth mode, $\hat{\mathbf{r}}_{ij}$ is the unit vector parallel to the mth bond. S is closer to unity when the mode of vibration is predominantly of bond-stretching type and will be close to 0 if the mode is of a bond-bending type. In Fig. 7, the region above 850 cm⁻¹ shows bond-stretching character, and the region below 850 cm⁻¹ can be further divided into two (not so obvious) regions; modes below 400 cm⁻¹ have bond-bending character and the region 400–850 cm⁻¹ shows a mixture of stretching and bending character (see Fig. 7 (d)).

The vibrational signatures were also analyzed using the phase quotient. This involves determining whether the atomic vibrations are in phase (acoustic) or out of phase (optical) in their nearest-neighbor local environment. The definition of phase quotient (q_p) is summarized as [50,51]:

$$q_p = \frac{1}{N_b} \frac{\sum_m \mathbf{u}_p^i \cdot \mathbf{u}_p^j}{\sum_m |\mathbf{u}_p^i \cdot \mathbf{u}_p^j|} \quad (4)$$

where, N_b is the number of valance bonds, \mathbf{u}_p^i and \mathbf{u}_p^j are the normalized displacement vectors (see Eq. (2)) for the pth normal mode. i sums over all the Si atoms and j enumerates neighboring atoms of one type (Si or O atom) of the ith atom.

A purely acoustic motion will have a value of 1, while the optic-like modes will attain a negative value for the phase quotient. Fig. 8 shows the phase quotient for $x = 1.3$ (Fig. 8 (a)), $x = 1.5$ (Fig. 8 (b)) and $x = 1.7$ (Fig. 8 (c)) for Si-O (in red) and Si-Si (in gray) nearest neighbors. To put things into perspective, for a crystalline solid, a given mode could appear to be completely acoustic (optical) in character when viewed from one symmetry (or another symmetry) direction, hence plots in Fig. 8 show the amorphous nature of a-SiO_x. The results obtained for the phase quotient are consistent with those observed from the stretch-bending behavior. From Fig. 8, the Si-Si vibrations appear to try to remain acoustic at all frequencies, while Si-O vibrations are acoustic at low frequencies and tend more towards optical vibrations at higher frequencies. The critical points in the Si-Si vibrations are consistent with the intermediate region described for stretch-bending behavior and indicate a mixture of both optical and acoustic behavior in the Si-Si vibrations.

3.3. Electronic structure and conduction

In Fig. 9, the states near the Fermi level (E_f ; shifted to 0) for each a-SiO_x model were analyzed by calculating the total electronic density of states (EDoS; black line). The localization in those states was calculated as the corresponding electronic inverse participation ratio (EIPR; green lines, see equation in ref. [52]). The EDoS for a-SiO_{1.7} shows a gap around the Fermi level, which suggests that it is non-conducting. For $x = 1.3$ and 1.5, the EIPR shows that the states in the valence and conduction tail regions are localized, indicating that electronic conduction occurs primarily by hopping mechanisms between those localized states [53]. Fig. S3 shows the EDoS projected on atomic sites. The peak of the Si 2p states (blue lines) near the Fermi level, which are attributed to the under-coordinated Si atoms in the network, is negatively correlated with x . This would imply that the under-coordinated Si atoms substantially contribute to the band-tail state. Fig. 10 confirms that a large fraction of under-coordinated Si atoms (in yellow) contribute to the localized states between ± 1 eV around E_f . In Fig. 10, the localization of each atom can be visually gauged by their size; the atoms with larger radii are more localized. O atoms are colored in black. Some of the IV-Si atoms also contribute (in a small fraction) to the band-tail states, which is due to the distortions in the bond length and/or angle [54].

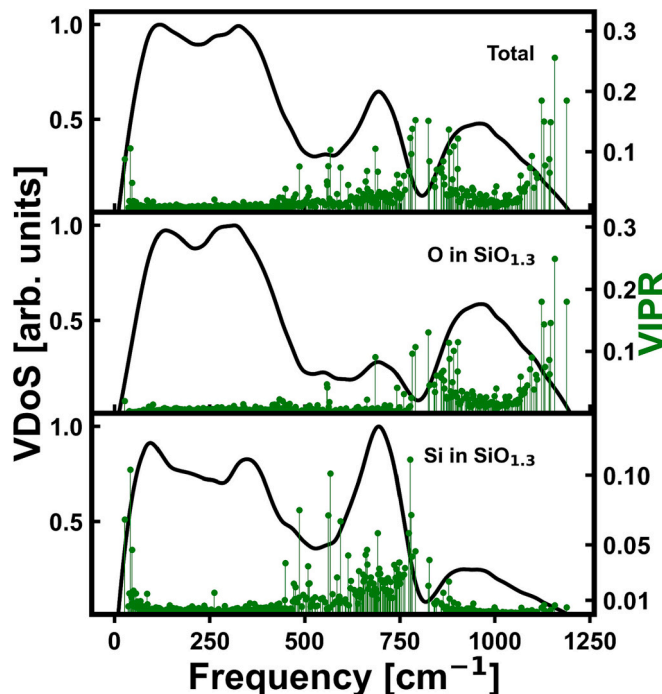


Fig. 6. The VDoS (in black) and VIPR (in green) for SiO_{1.3}.

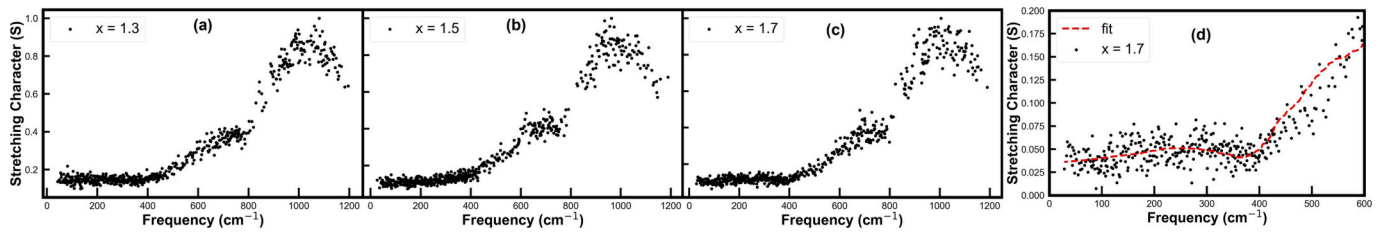


Fig. 7. Stretching character (S) versus the frequency for a-SiO_x models ($x =$ (a) 1.3, (b) 1.5, and (c) 1.7). The low (high) frequency range corresponds to acoustic, bond-bending (optical, stretching) modes. The low frequency modes behaviour around 400 cm⁻¹ for $x = 1.7$ is shown in d.

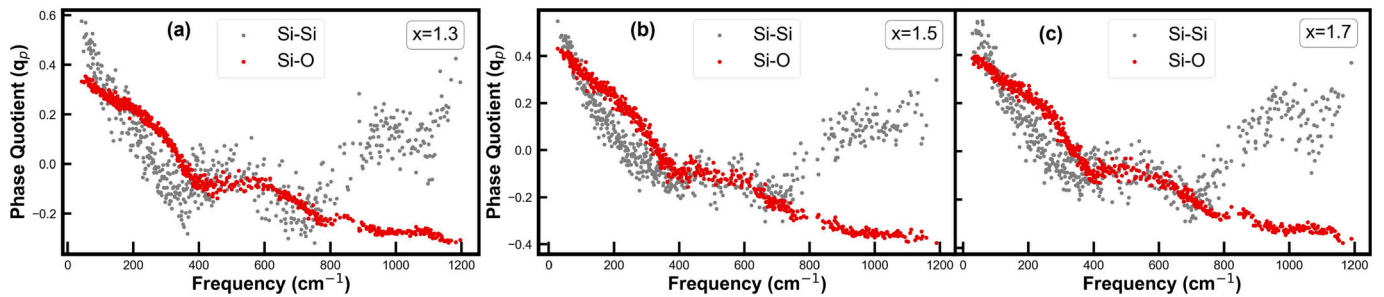


Fig. 8. Phase Quotient (q_p) versus the frequency for a-SiO_x models. (a) $x = 1.3$, (b) $x = 1.5$, and (c) $x = 1.7$.

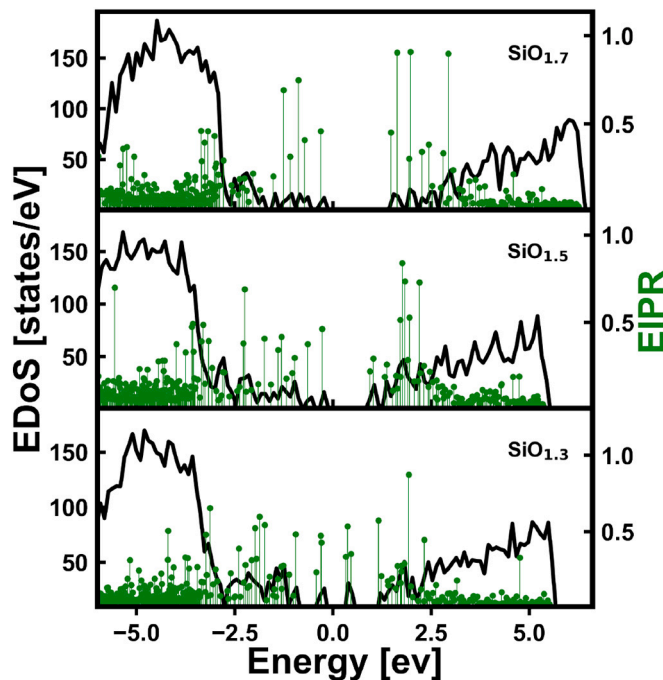


Fig. 9. Electronic density of states (EDoS) and the electronic inverse participation ratio (EIPR) for a-SiO_x models. The Fermi level has been shifted to 0.

Several theoretical models focusing on electronic transport in amorphous dielectrics have been developed over the years [55–57]. One of these models is based on the idea of threshold connectivity from the percolation theory of Broadbent and Hammersley [58]. Another similar approach (for SiO_x) is the nanoscale potential fluctuation model of Peravalov and co-workers [40]. Using a core-shell model, they proposed that Si nanoclusters act as potential wells for electrons and holes in the SiO_x matrix, resulting in a percolation mechanism of charge transport [59]. For this work, the electronic transport in SiO_x is treated within the space-projected conductivity (SPC) formalism [22,60], an *ab initio* method that describes the electronic conductivity in spatial grids based

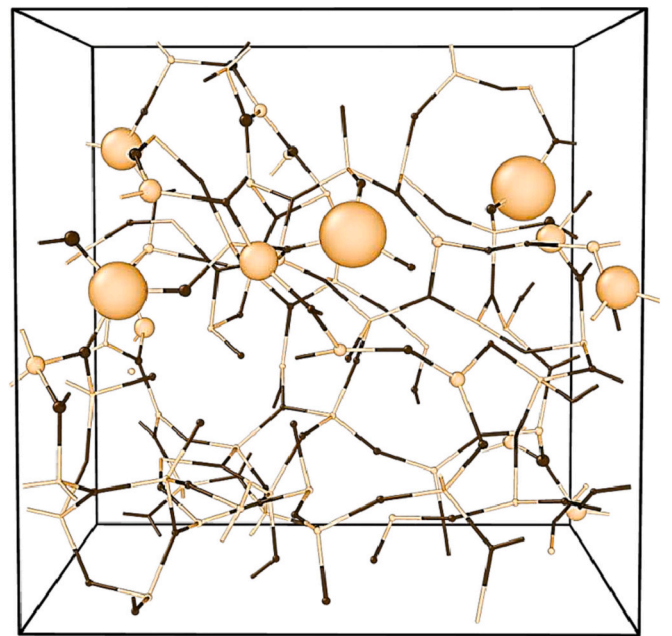


Fig. 10. Atoms associated with localized electronic states ± 1 eV around the Fermi level. The contribution of each atom can be visually gauged by their size; atoms with a large radius are more localized than those having a smaller radius. Si (O) atoms are colored yellow (black). Some atoms were manually deleted to allow optimal visualization of the localized atoms.

on realistic atomic configuration obtained from accurate inter-atomic forces, Kohn–Sham single particle states and the Kubo–Greenwood formula for electrical conductivity [61,62]. SPC has been successfully applied in studying the electronic conductivity in liquids, amorphous materials, and mixed systems [63–66]. For SPC calculations, the diagonal elements of the conductivity tensor for each k -point (k) and frequency (ω) are applied in the standard Kubo–Greenwood formula given as [61,62]:

$$\sigma_{\mathbf{k}}(\omega) = \frac{2\pi e^2}{3m^2\omega\Omega} \sum_{ij} \sum_{\alpha} [f(\epsilon_{i,\mathbf{k}}) - f(\epsilon_{j,\mathbf{k}})] |\langle \psi_{j,\mathbf{k}} | p^{\alpha} | \psi_{i,\mathbf{k}} \rangle|^2 \delta(\epsilon_{j,\mathbf{k}} - \epsilon_{i,\mathbf{k}} - \hbar\omega) \quad (5)$$

where e and m represent the charge and mass of the electron respectively. Ω represents the volume of the supercell. The average over the diagonal elements of conductivity tensor ($\alpha = x, y, z$) is calculated, and $\psi_{i,\mathbf{k}}$ is the Kohn–Sham orbital associated with energy $\epsilon_{i,\mathbf{k}}$. The parameter $f(\epsilon_{i,\mathbf{k}})$ denotes the Fermi–Dirac weight and p^{α} is the momentum operator along each Cartesian direction α .

Defining a variable, $g_{ij}(\mathbf{k}, \omega)$ and suppressing the explicit dependence of σ on \mathbf{k} and ω as:

$$g_{ij}(\mathbf{k}, \omega) = \frac{2\pi e^2}{3m^2\omega\Omega} [f(\epsilon_{i,\mathbf{k}}) - f(\epsilon_{j,\mathbf{k}})] \delta(\epsilon_{j,\mathbf{k}} - \epsilon_{i,\mathbf{k}} - \hbar\omega) \quad (6)$$

The conductivity can then be expressed as:

$$\sigma = \sum_{ij,\alpha} g_{ij} \int d^3x \int d^3x' [\psi_j^*(x) p^{\alpha} \psi_i(x)] [\psi_j^*(x') p^{\alpha} \psi_i(x')]^* \quad (7)$$

Taking $\xi_{ji}^{\alpha}(x) = \psi_j^*(x) p^{\alpha} \psi_i(x)$ as a complex-valued function defined on the real-space grid (call them \mathbf{x}) with uniform grid size (h) in three dimensions makes it possible to approximate the integrals as a sum on the grid from Eq. (7), which is then rewritten as:

$$\sigma \approx h^6 \sum_{x,x'} \sum_{ij,\alpha} g_{ij} \xi_{ji}^{\alpha}(x) (\xi_{ji}^{\alpha}(x'))^* \quad (8)$$

In Eq. (8), the approximation becomes exact as $h \rightarrow 0$. If $\Gamma(x, x')$ is a Hermitian, positive-semidefinite matrix, then it can be expressed as:

$$\Gamma(x, x') = \sum_{ij,\alpha} g_{ij} \xi_{ji}^{\alpha}(x) (\xi_{ji}^{\alpha}(x'))^* \quad (9)$$

This allows the total conductivity to be expressed as:

$$\sigma = \sum_x \Gamma(x, x) + \sum_{x,x', x \neq x'} \Gamma(x, x') \quad (10)$$

From which the SPC (ζ) is computed as:

$$\zeta(x) = \left| \sum_{x'} \Gamma(x, x') \right| \quad (11)$$

To implement the method, the supercell was divided into $40 \times 40 \times 40$ ($\dim \Gamma = 64000$) grid points. The wave functions are the Kohn–Sham orbitals $\Psi_{i\mathbf{k}}$ computed within VASP. The gradient of ψ_i for each α was

computed using the central-finite difference method. A temperature of 1000 K was used in calculating the Fermi–Dirac distribution function. In this work, only $\mathbf{k} = \mathbf{0}$ was considered.

Fig. 11 shows the isosurface plots of SPC (yellow blobs) for a-SiO_x models. The occupancy of the states was estimated assuming that the Fermi level lies at the midpoint of HOMO and LUMO levels (intrinsic case). The conductivity path strongly favored Si–Si connections in the network for all the models. A few IV–Si atoms with strained tetrahedra SiO₂ were found to also form active sites for charge trapping and they, therefore, contribute to the conductivity; however, such contributions were rare when compared to those from the O-vacancy sites. For SiO_{1.7}, as indicated in Fig. 9, the majority of O-vacancy sites are localized away from the Fermi level and hence, they do not contribute to the conduction. This is why Fig. 11 (a) shows localized conductivity in the dissociated O-vacancy sites that do not form any conduction path. For SiO_{1.3} and SiO_{1.5} in Fig. 11 (b) and (c) respectively, a few under-coordinated Si atoms also form charge-trapping sites, and the combination of tri-vacancy chains in Si-rich regions provides a conductivity path where conduction likely occurs via trap-assisted tunneling (TAT) mechanism [67–69]. It should be noted that the consequence of the finite size of the models is that electronic states considered in the SPC calculations are few; hence, the conductivity is mostly qualitative. However, the randomness in the local atomic conformation in all the aSiO_x models considered provided a satisfactory estimate of the optimal conduction path to be along regions with O-vacancy sites connected to form member rings or vacancy chains. Additionally, the unique conduction path formed for each $x = 1.3$ and 1.5 model satisfies the primary requirement for PUFs.

Another area of interest is the modulation of electronic transport through doping. Doping was crudely modeled by shifting the Fermi level of the models towards the valence and conduction band-tail regions where comparatively there are more states than in the intrinsic case discussed earlier. SPC was computed for these two cases and displayed as isosurface plots in Fig. 12 for the a-SiO_{1.3} model presented in Fig. 11. The [TOP] and [BOTTOM] plots correspond to the Fermi level shifted to the valence-tail (p-doped) and the conduction-tail (n-doped) region respectively. In the intrinsic case (Fig. 11), the density of deep states is relatively low in the mid-gap region and the conduction zones are not well connected. This was considerably improved by doping, resulting in longer electronic conduction paths in Fig. 12. The conduction-active path remains primarily along the Si–Si connections in the network for both the p-doped and n-doped configurations. Still, not all of these O-vacancy sites form conduction paths and may only serve as charge-trapping sites in the network. The notable difference in the conduction path for the n-type and p-type shows that the conduction path obtained via doping is not unique but rather depends on the choice of the Fermi

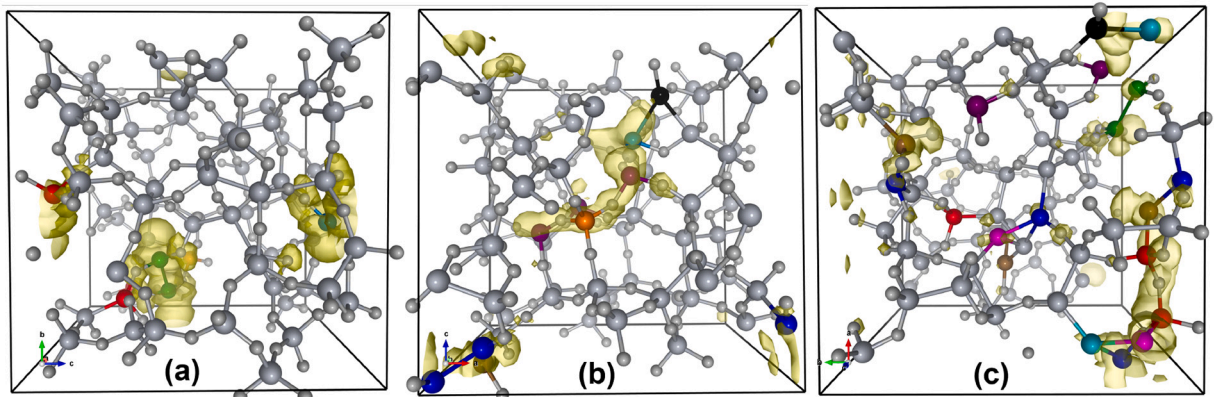


Fig. 11. Isosurface plots showing SPC (yellow colored blobs) for intrinsic a-SiO_x models for (a) $x = 1.7$, (b) $x = 1.5$ and (c) $x = 1.3$ respectively. The Si atoms within the conduction-active region are color-coded the same as in Fig. 4. The conductivity values up to 40% of the highest value are considered in each plot. The remaining Si and O atoms are shown in gray color, and O atoms are represented by smaller spheres.

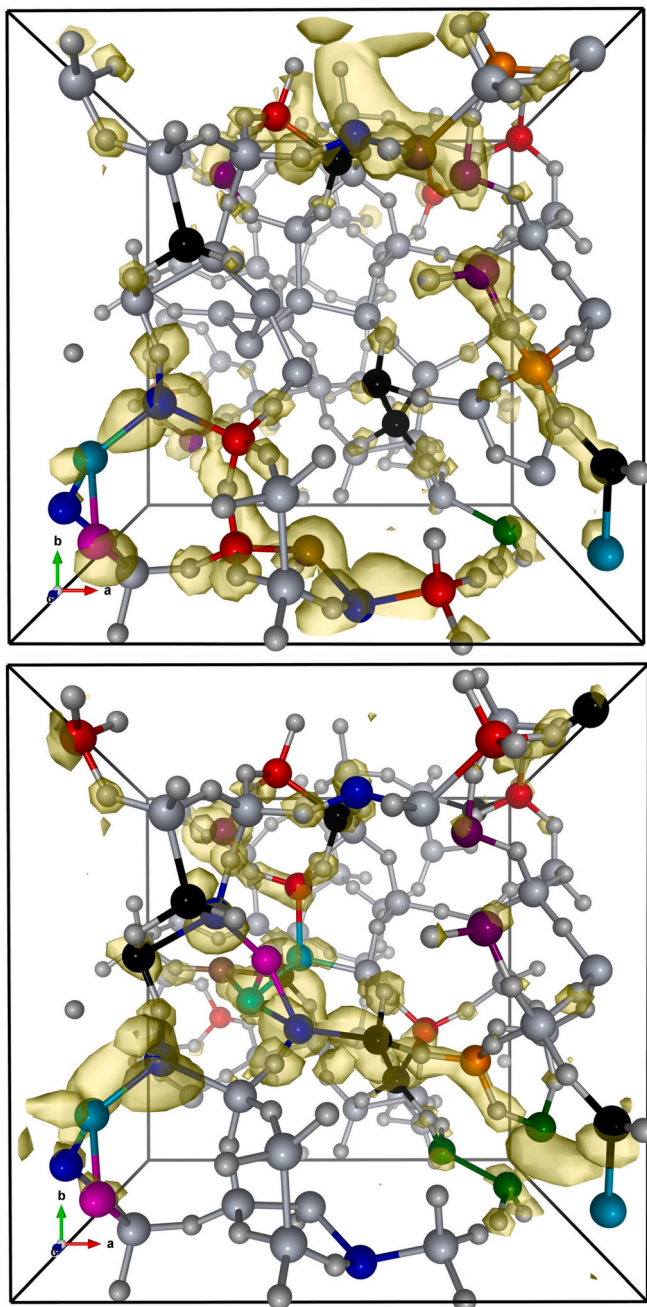


Fig. 12. Isosurface plots (yellow-colored blob) showing SPC for $x = 1.3$ model with shifted by 2 eV on both sides from the intrinsic Fermi level (i.e., 0 eV in Fig. 9). TOP: Valence-tail region (Fermi level at ≈ -2.0 eV) and BOTTOM: Conduction-tail region (Fermi level at ≈ 2 eV). The cutoff up to 0.04 times the highest value is considered. The colors of the atoms are as discussed in Fig. 11.

level shift, which changes the occupancy of the electronic state, and by extension, the conduction path. The ability to switch the conduction path in the material based on the available O-vacancy sites and doping in the network is a useful property for PUFs. While these analyses confirm that low x sub-stoichiometric silicon suboxides are optimal for PUFs; this does not imply that lower x structures (like $x = 0.5, 1, \dots$) are desirable for PUF fabrication. Despite obtaining longer conductivity paths with lower x sub-stoichiometric silicon oxides, the practical requirement of variations in the conduction path for individual PUFs embodied in solid-state devices will not be met.

4. Conclusions

In this work, the electronic transport of sub-stoichiometric silicon suboxides (SiO_x ; $x = 1.3, 1.5$ and 1.7) used in Physical Unclonable Functions (PUFs) was investigated using the space-projected conductivity formalism. Atomistic models of $\alpha\text{-SiO}_x$ were obtained using molecular dynamics with Tersoff potential followed by DFT energy minimization. The connection between the structure, electronic, and vibration properties of $\alpha\text{-SiO}_x$ to the electronic conduction was discussed. It was observed that different tetrahedral structures in the models could represent different O-vacancy sites. The electronic structure of the models, calculated via the electronic density of states and inverse participation ratio, showed that Si atoms were mostly localized electronic states near the Fermi level. Vibration signatures of $\alpha\text{-SiO}_x$ have peaks at $\approx 900 \text{ cm}^{-1}$ which are due to the non-bridging oxygen atoms. Space-projected conductivity (SPC) calculations inferred that the O-vacancy sites contribute to the electronic transport, and shifting the Fermi level towards the valence and conduction-tail regions (in an attempt to simulate doping) confirmed that the conduction path varies with O-vacancy sites. The combined properties investigated for $\alpha\text{-SiO}_x$ make this material a promising candidate for PUF devices.

CRediT authorship contribution statement

C. Ugwumadu: Conceptualization, Methodology, Software, Writing-original-draft, Writing-review-editing, Formal-analysis, Visualization. **K.N. Subedi:** Conceptualization, Methodology, Software, Writing-original-draft, Writing-review-editing, Formal-analysis, Visualization. **R. Thapa:** Software, Validation, Writing-review-editing. **P. Apsangi:** Methodology, Validation, Investigation. **S. Swain:** Methodology, Validation, Investigation. **M.N. Kozicki:** Supervision, Project-administration, Funding-acquisition, Writing-original-draft, Writing-review-editing. **D.A. Drabold:** Supervision, Project-administration, Funding-acquisition, Writing-original-draft, Writing-review-editing.

Declaration of Competing Interest

The authors declare that they have no known competing financial interests or personal relationships that could have appeared to influence the work reported in this paper.

Data availability

Data will be made available on request.

Acknowledgments

The authors acknowledge Prof. Sumit Sharma and Mr. Clay Burger for their helpful advice during the course of this work. They also thank Ms. Anna-Theresa Kirchttag for proofreading the manuscript, the National Science Foundation (NSF) for support for the PUF fabrication under Grant No. 1827753, and XSEDE (supported by NSF Grant No. ACI-1548562) for computational support under Allocation No. DMR-190008P.

Appendix A. Supplementary data

Supplementary data associated with this article can be found, in the online version, at <https://doi.org/10.1016/j.nocx.2023.100179>.

References

- [1] M. El-hajj, A. Fadlallah, M. Chamoun, A. Serhrouchni, A Survey of Internet of Things (IoT) Authentication Schemes, *Sensors* 19 (5) (2019), <https://doi.org/10.3390/s19051141>. URL:<https://www.mdpi.com/1424-8220/19/5/1141>.

- [2] S. Skorobogatov, Hardware Security Implications of Reliability, Remanence and Recovery in Embedded Memory, in: DAC conference, PAINE workshop, vol. 2, 2018, pp. 314–321. doi:10.17863/CAM.28103.
- [3] R. Maes, Physically Unclonable Functions: Constructions, Properties and Applications, first ed., Springer, Berlin, Heidelberg, 2013.
- [4] B.C. Grubel, B.T. Bosworth, M.R. Kossey, H. Sun, A.B. Cooper, M.A. Foster, A. C. Foster, Silicon photonic physical unclonable function, *Opt. Express* 25 (11) (2017) 12710–12721, <https://doi.org/10.1364/OE.25.012710>. URL:<http://opg.optica.org/oe/abstract.cfm?URI=oe-25-11-12710>.
- [5] D.-I. Moon, A. Rukhin, R.P. Gandhiraman, B. Kim, S. Kim, M.-L. Seol, K.J. Yoon, D. Lee, J. Koehne, J.-W. Han, M. Meyyappan, Physically Unclonable Function by an All-Printed Carbon Nanotube Network, *ACS Appl. Electron. Mater.* 1 (7) (2019) 1162–1168, <https://doi.org/10.1021/acsaelm.9b00166>.
- [6] M. Kozicki, Physical unclonable functions with silicon-rich dielectric devices, *US Patent App.* 17/112,668 (Jun. 10 2021).
- [7] W. Chen, S. Tappertzhofen, H.J. Barnaby, M.N. Kozicki, SiO₂ based conductive bridging random access memory, *J. Electroceram.* 39 (2017) 109–131.
- [8] G. Wang, Y. Yang, J.-H. Lee, V. Abramova, H. Fei, G. Ruan, E.L. Thomas, J.M. Tour, Nanoporous silicon oxide memory, *Nano Lett.* 14 (8) (2014) 4694–4699, <https://doi.org/10.1021/nl501803s>, PMID: 24992278. arXiv:<https://doi.org/10.1021/nl501803s>.
- [9] Y.-F. Chang, P.-Y. Chen, B. Fowler, Y.-T. Chen, F. Xue, Y. Wang, F. Zhou, J.C. Lee, Understanding the resistive switching characteristics and mechanism in active SiO_x-based resistive switching memory, *J. Appl. Phys.* 112 (12) (2012), 123702.
- [10] A. Mehonic, M. Buckwell, L. Montesi, L. Garnett, S. Fearn, R. Chater, D. McPhail, A.J. Kenyon, Structural changes and conductance thresholds in metal-free intrinsic SiO_x resistive random access memory, *J. Appl. Phys.* 117 (12) (2015), 124505.
- [11] A. Mehonic, M. Munde, W. Ng, M. Buckwell, L. Montesi, M. Bosman, A. Shluger, A. Kenyon, Intrinsic resistance switching in amorphous silicon oxide for high performance SiO_x ReRAM devices, *Microelectron. Eng.* 178 (2017) 98–103, special issue of Insulating Films on Semiconductors (INFOS 2017).
- [12] T.V. Perevalov, V.A. Volodin, G.N. Kamaev, A.A. Gismatulin, S.G. Cherkova, I. P. Prosvirin, K.N. Astankova, V.A. Gritsenko, Electronic structure of silicon oxynitride films grown by plasma-enhanced chemical vapor deposition for memristor application, *J. Non-Cryst. Solids* 598 (2022), 121925, <https://doi.org/10.1016/j.jnoncrysol.2022.121925>. URL:<https://www.sciencedirect.com/science/article/pii/S0022309322005208>.
- [13] S.H. Jo, K.-H. Kim, W. Lu, Programmable Resistance Switching in Nanoscale Two-Terminal Devices, *Nano Lett.* 9 (1) (2009) 496–500.
- [14] S.H. Jo, W. Lu, CMOS Compatible Nanoscale Nonvolatile Resistance Switching Memory, *Nano Lett.* 8 (2) (2008) 392–397.
- [15] J. Yao, Z. Sun, L. Zhong, D. Natelson, J.M. Tour, Resistive Switches and Memories from Silicon Oxide, *Nano Lett.* 10 (10) (2010) 4105–4110.
- [16] A. Mehonic, S. Cuffe, M. Wojdak, S. Hudziak, O. Jambois, C. Labbé, B. Garrido, R. Rizk, A.J. Kenyon, Resistive switching in silicon suboxide films, *J. Appl. Phys.* 111 (7) (2012), 074507.
- [17] M.N. Kozicki, H.J. Barnaby, Conductive bridging random access memory—materials, devices and applications, *Semicond. Sci. Technol.* 31 (11) (2016), 113001, <https://doi.org/10.1088/0268-1242/31/11/113001>.
- [18] I. Valov, R. Waser, J.R. Jameson, M.N. Kozicki, Electrochemical metallization memories—fundamentals, applications, prospects, *Nanotechnology* 22 (25) (2011), 254003, <https://doi.org/10.1088/0957-4484/22/25/254003>.
- [19] L.-G. Wang, X. Qian, Y.-Q. Cao, Z.-Y. Cao, G.-Y. Fang, A.-D. Li, W. Di, Excellent resistive switching properties of atomic layer-deposited Al₂O₃/HfO₂/Al₂O₃ trilayer structures for non-volatile memory applications. *Nanoscale Res. Lett.* 10 (135) (2015) <https://doi.org/10.1186/s11671-015-0846-y>.
- [20] W. Chen, R. Fang, M.B. Balaban, W. Yu, Y. Gonzalez-Velo, H.J. Barnaby, M. N. Kozicki, A CMOS-compatible electronic synapse device based on Cu/SiO₂/W programmable metallization cells, *Nanotechnology* 27 (25) (2016), 255202, <https://doi.org/10.1088/0957-4484/27/25/255202>.
- [21] K. Subedi, Theory of electronic transport and novel modeling of amorphous materials, Ph.D. thesis (2022). URL:https://etd.ohiolink.edu/apexprod/rws_oli/nk/r/1501/10?clear=10&p10_accession_num=ohiou1640014277883479.
- [22] K.N. Subedi, K. Prasai, D.A. Drabold, Space-projected conductivity and spectral properties of the conduction matrix, *Phys. Status Solidi (B)* 258 (9) (2021), <https://doi.org/10.1002/pssb.202000438>. URL:<https://onlinelibrary.wiley.com/doi/abs/10.1002/pssb.202000438>. arXiv:<https://onlinelibrary.wiley.com/doi/pdf/10.1002/pssb.202000438>.
- [23] D.A. Drabold, Topics in the theory of amorphous materials, *Eur. Phys. J. B* 68 (2009) 1–21.
- [24] S. Munetoh, T. Motooka, K. Moriguchi, Tersoff-style three-body potential for SiO developed by Munetoh et al. (2007) v000, OpenKIM, <https://doi.org/10.25950/59df4e98> (2022). doi:10.25950/59df4e98.
- [25] S. Munetoh, T. Motooka, K. Moriguchi, A. Shintani, Interatomic potential for Si-O systems using Tersoff parameterization, *Comput. Mater. Sci.* 39 (2) (2007) 334–339, <https://doi.org/10.1016/j.commatsci.2006.06.010>. URL:<https://www.sciencedirect.com/science/article/pii/S0927025606002023>.
- [26] Y. Akio, Using an extended tersoff interatomic potential to analyze the static-fatigue strength of SiO₂ under atmospheric influence, *JSME Int. J. Ser. A, Mech. Mater. Eng.* 39 (3) (1996) 313–320.
- [27] B.S. R. C. Alessandro, F. Dominik, A. Wanda, *Ab initio* derived augmented tersoff potential for silicon oxynitride compounds and their interfaces with silicon, *Phys. Rev. B* 73 (15) (2006), 155329.
- [28] H. Gu, J. Wang, X. Wei, H. Wang, Z. Li, Thermal conductivity and interfacial thermal resistance in the heterostructure of silicon/amorphous silicon dioxide: the strain and temperature effect, *Nanotechnology* 31 (50) (2020), 505703, <https://doi.org/10.1088/1361-6528/abb504>.
- [29] H. Akihiko, K. Shinji, A. Toshihiro, A. Masazumi, Y. Chihiro, I. Hideto, T. Yongwen, F. Takeshi, C. Mingwei, Atomic-scale disproportionation in amorphous silicon monoxide, *Nat. Commun.* 7 (1) (2016) 1–7.
- [30] A. Barranco, F. Yubero, J.P. Espinós, P. Groening, A.R. González-Elipe, Electronic state characterization of SiO_x thin films prepared by evaporation, *J. Appl. Phys.* 97 (11) (2005), 113714.
- [31] A.P. Thompson, H.M. Aktulga, R. Berger, D.S. Bolintineanu, W.M. Brown, P. S. Crozier, P.J. in 't Veld, A. Kohlmeyer, S.G. Moore, T.D. Nguyen, R. Shan, M. J. Stevens, J. Tranchida, C. Trit, S.J. Plimpton, LAMMPS - a flexible simulation tool for particle-based materials modeling at the atomic, meso, and continuum scales, *Comput. Phys. Commun.* 271 (2022) 108171, <https://doi.org/10.1016/j.cpc.2021.108171>. URL:<https://www.sciencedirect.com/science/article/pii/S0010465521002836>.
- [32] S. Nosé, A unified formulation of the constant temperature molecular dynamics methods, *J. Chem. Phys.* 81 (1) (1984) 511–519.
- [33] N. Shuichi, Constant temperature molecular dynamics methods, *Prog. Theor. Phys. Suppl.* 103 (1991) 1–46.
- [34] D.M. Bylander, L. Kleinman, Energy fluctuations induced by the Nosé thermostat, *Phys. Rev. B* 46 (1992) 13756–13761.
- [35] G. Kresse, J. Furthmüller, Efficient iterative schemes for *ab initio* total-energy calculations using a plane-wave basis set, *Phys. Rev. B* 54 (1996) 11169–11186, <https://doi.org/10.1103/PhysRevB.54.11169>. URL:<https://link.aps.org/doi/10.1103/PhysRevB.54.11169>.
- [36] J.P. Perdew, K. Burke, M. Ernzerhof, Generalized Gradient Approximation Made Simple, *Phys. Rev. Lett.* 77 (1996) 3865–3868, <https://doi.org/10.1103/PhysRevLett.77.3865>. URL:<https://link.aps.org/doi/10.1103/PhysRevLett.77.3865>.
- [37] R. Thapa, C. Ugwumadu, K. Nepal, D.A. Drabold, M.T. Shatnawi, *Ab initio* simulation of amorphous GeSe₃ and GeSe₄, *J. Non. Cryst. Sol.* 601 (2023) 121998, <https://doi.org/10.1016/j.jnoncrysol.2022.121998>.
- [38] Realistic models of binary glasses from models of tetrahedral amorphous semiconductors, De Nyago Tafan and D. A. Drabold, *Rev. B* 68 165208, doi: 10.1103/PhysRevB.68.165208.
- [39] A. Barranco, J.A. Mejias, J.P. Espinos, A. Caballero, A.R. Gonzalez-Elipe, F. Yubero, Chemical stability of Si⁴⁺ species in SiO_x (x<2) thin films, *J. Vac. Sci. Technol. A* 19 (1) (2001) 136–144, <https://doi.org/10.1116/1.1323972>.
- [40] T. Perevalov, V. Volodin, G. Kamaev, G. Krivyakin, V. Gritsenko, I. Prosvirin, Electronic structure and nanoscale potential fluctuations in strongly nonstoichiometric pcvd SiO_x, *J. Non-Cryst. Solids* 529 (2020) 119796, <https://doi.org/10.1016/j.jnoncrysol.2019.119796>. URL:<https://www.sciencedirect.com/science/article/pii/S0022309319306660>.
- [41] N.L. Anderson, R.P. Vedula, P.A. Schultz, R.M. Van Ginhoven, A. Strachan, First-principles investigation of low energy e⁻ center precursors in amorphous silica, *Phys. Rev. Lett.* 106 (20) (2011), 206402.
- [42] Y. Yue, Y. Song, X. Zuo, First principles study of oxygen vacancy defects in amorphous SiO₂, *AIP Adv.* 7 (1) (2017), 015309.
- [43] M.S. Manveer, G.Z. David, S.L. Alexander, Diffusion and aggregation of oxygen vacancies in amorphous silica, *J. Phys.: Condens. Matter* 29 (24) (2017), 245701.
- [44] D.Z. Gao, J. Strand, M.S. Munde, A.L. Shluger, Mechanisms of Oxygen Vacancy Aggregation in SiO₂ and HfO₂, *Front. Phys.* 7 (2019) 43.
- [45] C. Ugwumadu, K. Nepal, R. Thapa, D.A. Drabold, Atomistic nature of amorphous graphite, Physics and Chemistry of Glasses: European Journal of Glass Science and Technology Part B 64 (2023) 16, <https://doi.org/10.13036/17533562.64.1.18>.
- [46] B. Bhattarai, D. Drabold, Vibrations in amorphous silica, *J. Non-Cryst. Solids* 439 (2016) 6–14, <https://doi.org/10.1016/j.jnoncrysol.2016.02.002>. URL:<https://www.sciencedirect.com/science/article/pii/S0022309316300230>.
- [47] I. Simon, Structure of neutron-irradiated quartz and vitreous silica, *J. Am. Ceram. Soc.* 40 (5) (1957) 150–153.
- [48] R.J. Bell, P. Dean, On the Localized Vibrations of Non-Bridging Oxygen Atoms in Vitreous Silica, Springer, US, Boston, MA, 1968, pp. 124–131, https://doi.org/10.1007/978-1-4899-6445-8_13.
- [49] N. Zotov, I. Ebbsjö, D. Timpel, H. Keppeler, Calculation of Raman spectra and vibrational properties of silicate glasses: Comparison between Na₂Si₄O₉ and SiO₂ glasses, *Phys. Rev. B* 60 (1999) 6383–6397, <https://doi.org/10.1103/PhysRevB.60.6383>. URL:<https://link.aps.org/doi/10.1103/PhysRevB.60.6383>.
- [50] R.J. Bell, D.C. Hibbins-Butler, Acoustic and optical modes in vitreous silica, germania and beryllium fluoride, *J. Phys. C: Solid State Phys.* 8 (6) (1975) 787–792, <https://doi.org/10.1088/0022-3719/8/6/009>.
- [51] S.N. Taraskin, S.R. Elliott, Nature of vibrational excitations in vitreous silica, *Phys. Rev. B* 56 (1997) 8605–8622, <https://doi.org/10.1103/PhysRevB.56.8605>. URL:<https://link.aps.org/doi/10.1103/PhysRevB.56.8605>.
- [52] C. Ugwumadu, K. Nepal, R. Thapa, Y. Lee, Y. Al Majali, J. Tremblay, D.A. Drabold, Simulation of multi-shell fullerenes using Machine-Learning Gaussian Approximation Potential, *Carbon Trends* 10 (2023) 100239, <https://doi.org/10.1016/j.cartre.2022.100239>.
- [53] J. Li, D.A. Drabold, Electron hopping between localized states: A simulation of the finite-temperature anderson problem using density functional methods, *Phys. Rev. B* 68 (2003), 033103, <https://doi.org/10.1103/PhysRevB.68.033103>. URL:<https://link.aps.org/doi/10.1103/PhysRevB.68.033103>.
- [54] P.A. Fedders, D.A. Drabold, S.M. Nakhmanson, Theoretical study on the nature of band-tail states in amorphous Si, *Phys. Rev. B* 58 (1998) 15624–15631.
- [55] P. Borsenberger, L. Pautmeier, H. Bässler, Charge transport in disordered molecular solids, *J. Chem. Phys.* 94 (8) (1991) 5447–5454.

- [56] S. Baranovski, Charge transport in disordered solids with applications in electronics, John Wiley & Sons, 2006.
- [57] S. Baranovskii, O. Rubel, Charge transport in disordered materials, Springer Handbook of Electronic and Photonic Materials, 2017, 1–1.
- [58] S.R. Broadbent, J.M. Hammersley, Percolation processes: I. crystals and mazes, in: Mathematical proceedings of the Cambridge philosophical society, vol. 53, Cambridge University Press, 1957, pp. 629–641.
- [59] B.I. Shklovskii, A.L. Efros, Percolation theory and conductivity of strongly inhomogeneous media, Sov. Phys. Uspekhi 18 (11) (1975) 845, <https://doi.org/10.1070/PU1975v018n11ABEH005233>.
- [60] K. Prasai, K.N. Subedi, K. Ferris, P. Biswas, D.A. Drabold, Spatial Projection of Electronic Conductivity: The Example of Conducting Bridge Memory Materials, Phys. Status Solidi (RRL) – Rapid Res. Lett. 12 (9) (2018), 1800238, <https://doi.org/10.1002/pssr.201800238> arXiv:<https://onlinelibrary.wiley.com/doi/pdf/10.1002/pssr.201800238> URL:<https://onlinelibrary.wiley.com/doi/abs/10.1002/pssr.201800238>.
- [61] R. Kubo, Statistical-Mechanical Theory of Irreversible Processes. I. General Theory and Simple Applications to Magnetic and Conduction Problems, J. Phys. Soc. Jpn. 12 (6) (1957) 570–586, <https://doi.org/10.1143/JPSJ.12.570>, arXiv:<https://doi.org/10.1143/JPSJ.12.570>.
- [62] D.A. Greenwood, The Boltzmann Equation in the Theory of Electrical Conduction in Metals, Proc. Phys. Soc. 71 (4) (1958) 585–596, <https://doi.org/10.1088/0370-1328/71/4/306>.
- [63] K.N. Subedi, K. Prasai, M.N. Kozicki, D. A. Drabold, Structural origins of electronic conduction in amorphous copper-doped alumina, Phys. Rev. 3 (2019), 065605, <https://doi.org/10.1103/PhysRevMaterials.4.064603>.
- [64] R. Thapa, C. Ugwumadu, K. Nepal, J. Trembly, D.A. Drabold, Ab initio simulation of amorphous graphite, Phys Rev Lett. 128 (2022) 236402, <https://doi.org/10.1103/PhysRevLett.128.236402>.
- [65] C. Ugwumadu, R. Thapa, Y. Al-Majali, J. Trembly, D.A. Drabold, Formation of Amorphous Carbon Multi-Walled Nanotubes from Random Initial Configurations, Phys. Status Solidi B 260 (2023) 2200527, <https://doi.org/10.1002/pssb.202200527>.
- [66] K. Subedi, K. Nepal, C. Ugwumadu, K. Kappagantula, D.A. Drabold, Electronic transport in copper graphene composites, Applied Physics Letters 122 (2023), 031903, <https://doi.org/10.1063/5.0137086>.
- [67] S.M. Sze, Y. Li, K.K. Ng, Physics of semiconductor devices, John Wiley & sons, 2021.
- [68] J. Frenkel, On Pre-Breakdown Phenomena in Insulators and Electronic Semiconductors, Phys. Rev. 54 (1938) 647–648, <https://doi.org/10.1103/PhysRev.54.647> URL:<https://link.aps.org/doi/10.1103/PhysRev.54.647>.
- [69] S. Prezioso, A. Anopchenko, Z. Gaburro, L. Pavesi, G. Pucker, L. Vanzetti, P. Bellutti, Electrical conduction and electroluminescence in nanocrystalline silicon-based light emitting devices, J. Appl. Phys. 104 (6) (2008), 063103, <https://doi.org/10.1063/1.2977749> arXiv.